

Mid-InfraRed Outbursts in Nearby Galaxies (MIRONG). II. Optical Spectroscopic Follow-up

YIBO WANG,^{1,2} NING JIANG,^{1,2} TINGGUI WANG,^{1,2} LIN YAN,³ ZHENFENG SHENG,^{1,2} LIMING DOU,⁴ JIANI DING,⁵ ZHENG CAI,⁶
LUMING SUN,⁷ CHENWEI YANG,⁸ AND XINWEN SHU⁷

¹CAS Key Laboratory for Research in Galaxies and Cosmology, Department of Astronomy, University of Science and Technology of China, Hefei, 230026, China; wybustc@mail.ustc.edu.cn, jnac@ustc.edu.cn, shengzf@ustc.edu.cn, twang@ustc.edu.cn

²School of Astronomy and Space Sciences, University of Science and Technology of China, Hefei, 230026, China

³Caltech Optical Observatories, California Institute of Technology, Pasadena, CA 91125, USA; lyan@caltech.edu

⁴Department of Astronomy, Guangzhou University, Guangzhou 510006, China; doulm@gzhu.edu.cn

⁵Department of Astronomy and Astrophysics, UCO/Lick Observatory, University of California, 1156 High Street, Santa Cruz, CA 95064, USA

⁶Department of Astronomy, Tsinghua University, Beijing 100084, People's Republic of China

⁷Department of Physics, Anhui Normal University, Wuhu, Anhui, 241000, People's Republic of China

⁸Polar Research Institute of China, 451 Jinqiao Road, Shanghai, 200136, People's Republic of China

(Received 2021 August 31; Revised 2021 October 13; Accepted 2021 October 25)

Submitted to ApJS

ABSTRACT

Infrared echo has proven to be an effective means to discover transient accretion events of supermassive black holes (SMBHs), such as tidal disruption events (TDEs) and changing-look active galactic nuclei (AGNs), in dusty circumnuclear environments. To explore the dusty populations of SMBH transient events, we have constructed a large sample of Mid-infrared Outbursts in Nearby Galaxies (MIRONG) and performed multi-wavelength observations. Here we present the results of multiepoch spectroscopic follow-up observations of a subsample of 54 objects spanning a time scale of 4 yr. Emission-line variability was detected in 22 of them with either emergence or enhancement of broad Balmer emission lines in comparison with pre-outburst spectra. Coronal lines, He II λ 4686 and Bowen line N III λ 4640 appeared in the spectra of nine, seven and two sources, respectively. These results suggest that MIRONG is a mixed bag of different transient sources. We have tentatively classified them into different subclass according to their spectral evolution and light curves. Two sources have been in a steady high broad H α flux up to the latest observation and might be turn-on AGNs. Broad lines faded out in the remaining sources, indicating a transient ionizing source ignited by TDE or sporadic gas accretion. Thirty-one sources do not show noticeable spectral change with respect to their pre-outburst spectra. They have a statistically redder MIR color and lower MIR luminosity of the outbursts, which are consistent with heavily obscured events.

Keywords: galaxies: sample — galaxies: active — galaxies: nuclei

1. INTRODUCTION

Time-domain astronomy, which is promoted by wide-field, deep and fast surveys, has experienced great progress recently and resulted in the explosive growth of the discovery speed of various transients. Among them, the nuclear transients associated with supermassive black holes (SMBHs) have gradually become a regular class of targets in the past decade though their nature remains to be explored in many cases (e.g., Kankare et al. 2017; Trakhtenbrot et al. 2019; Hinkle et al. 2021; Malyali et al. 2021).

SMBHs are ubiquitous in the centers of massive galaxies. Most of them are inactive in the local universe (Kormendy &

Ho 2013). Occasionally, a dormant SMBH undergoes a temporary accretion phase when a star in the nucleus wanders within the tidal radius and gets torn apart. Part of the stellar debris will be accreted by the SMBH, producing a luminous flash of electromagnetic radiation peaked at soft X-ray to ultraviolet (UV) bands. The process is called a tidal disruption event (TDE; Rees 1988; Evans & Kochanek 1989; Phinney 1989).

Though predicted in the 1970s, the discovery of TDEs was not realized until the late 1990s (Bade et al. 1996) because their rarity makes the discovery rather challenging. First, the duration of a TDE is short, which normally rises to a peak

in \sim one month and then decays in months to years. Second, the event rate is as low as $10^{-4} - 10^{-5}$ /galaxy/year (Wang & Merritt 2004; Stone & Metzger 2016). The accumulated number of TDEs to date remains in two digits. Nevertheless large optical surveys, such as the Zwicky Transient Facility (ZTF), have greatly advanced the searching efficiency in the past few years (see review by Gezari 2021), and will eventually bring the field into the era of population study (van Velzen et al. 2021a). TDEs offer us a unique opportunity to probe SMBHs in normal galaxies (Lu et al. 2017; Mockler et al. 2019; Pasham et al. 2019) and the life cycle of accretion disks (e.g., Wevers et al. 2019) as well as jets (e.g., Bloom et al. 2011; Burrows et al. 2011; Mattila et al. 2018; Alexander et al. 2020).

In addition to TDEs, SMBHs may also experience sporadic gas accretion due to instability of the accretion flow or stochastic infall of cold gas clouds, such as G1/2 in the Galactic center. In some active galactic nuclei (AGNs), broad emission lines appear/disappear in response to the dramatic change of the central ionizing continuum on time scales from a few months to a few years. They are dubbed as "changing-look" AGNs (e.g., Shappee et al. 2014; LaMassa et al. 2015; MacLeod et al. 2016; Yang et al. 2018; Guo et al. 2019; Sheng et al. 2020). In the most extreme cases, a quiescent galaxy is transformed to an AGN or vice versa, called "turn-on" (Gezari et al. 2017; Frederick et al. 2019; Yan et al. 2019) or "turn-off" AGNs (e.g., Runnoe et al. 2016). The dramatic change of their accretion rate has already posed a serious challenge to canonical accretion disk theories. Moreover, the event rate statistics of changing-look AGNs may advance our knowledge of the AGN duty cycle, which might impact the evolution of their host galaxies via feedback.

Given the importance of TDEs and changing-look AGNs, a systematic search for them is a pressing need. The search hitherto has mainly focused on the optical band and yielded a mounting number of TDEs (e.g., van Velzen et al. 2020, 2021a) and turn-on AGNs (e.g., Frederick et al. 2019) discovered in real time, which allows prompt follow-up observations. However, the optical search is unavoidably affected by dust extinction and thus may overlook events in dusty environments. For instance, the low dust-covering factor of optical TDEs suggests that the optical band might be merely effective in unveiling TDEs in very dust-poor environments (Jiang et al. 2021b). Fortunately, obscured events may expose themselves as reprocessed infrared (IR) emission by dust in the vicinity of SMBHs (Lu et al. 2016), namely IR echoes of TDEs (Dou et al. 2016; Jiang et al. 2016; van Velzen et al. 2016, 2021b) and changing-look AGNs (Sheng et al. 2017), which are relatively transparent in the mid-infrared (MIR) to a moderately thick obscurer. Systematic searches in the IR have already led to successful discoveries of completely obscured TDEs (e.g., Mattila et al. 2018; Kool

et al. 2020). The other potential use of an IR search is its ability to reveal transients that are optically weak but luminous in higher-energy bands (e.g., UV and X-rays). Actually, classic TDE models predict emissions from accretion exactly in such wavelength regimes.

Encouraged by the powerful IR echoes (e.g., Wang et al. 2018a; Sheng et al. 2020), we have recently carried out a systematic search of ongoing outbursts in the MIR band using archival Wide-field Infrared Survey Explorer (WISE) light curves. We obtained a sample of 137 MIR outbursts in nearby galaxies (MIRONG) at $z < 0.35$, which showed a sudden brightening of > 0.5 mag in at least one WISE band (Jiang et al. 2021a, hereafter Paper I). The Majority of these MIRONG do not have any known corresponding optical flares, indicating dust extinction or intrinsic weakness in the optical band. Their MIR luminosities are markedly brighter than those of known supernovae (SNe) and their physical locations are very close to the galactic center (median $< 0''.1$), suggesting strongly that they are dust echoes of transient accretion events onto SMBHs. Multiwavelength follow-up observations have been undertaken since 2017 to investigate the nature of the newly unveiled MIRONG. In particular, their optical spectroscopic observations are a key part of the monitoring and can provide the most direct imprint of the outburst by probing the variability of characteristic emission lines.

This paper is the second one in the series of MIRONG and is dedicated specifically to the spectral evolution of MIRONG. We assume a cosmology with $H_0 = 70$ km s $^{-1}$ Mpc $^{-1}$, $\Omega_m = 0.3$, and $\Omega_\Lambda = 0.7$.

2. SAMPLE DESCRIPTION AND OBSERVATION STRATEGY

The spectroscopic sample was drawn from the parent MIRONG sample as described in Paper I. In order to capture potential spectral signals in a timely manner for rapidly evolving transients, such as TDEs, we select targets that are still in the early stage of the outburst for spectroscopic observations. Our observing campaign started in 2017 April, and a total of 54 objects have been observed up to 2021 March. The median redshift is 0.09, which is similar to the parent sample.

The observations were carried out with either the Double spectrograph (DBSP) mounted on the Hale 200 inch telescope at Palomar observatory (Oke & Gunn 1982) or the Kast DBSP on the Shane telescope at Lick observatory (Miller & Stone 1993). We adopt the D55 dichroic for Hale 200 inch telescope, which splits the incoming light into separate red and blue channels at 5500 Å for two different gratings, with a blue grism of 600 lines per mm blazed at 3780 Å and a red grism of 316 lines per mm blazed at 7150 Å. The slit width of 1'', 1.''5 or 2'' was used depending on the weather. Such

setup achieves a resolution of 5.23-10.46 Å in the red channel and 2.76-5.32 Å in the blue channel with a full spectral wavelength coverage of about 3100-10500 Å. With a proper exposure time chosen for each source, the median signal-to-noise ratios (S/N) are 14.2 pixel⁻¹ and 25.6 pixel⁻¹, respectively, for the blue- and red-end DBSP spectra. The Shane telescope was configured with a D57 dichroic, blue grism of 600 lines per mm blazed at 4130 Å, red grating of 600 lines per mm blazed at 7500 Å and slit widths of 1'' or 1.''5, which result in a resolution of 2.4-3.6 Å on the blue end and 3.0-4.5 Å on the red end and a full spectral wavelength coverage of about 3000-10000 Å. Slightly lower median S/N of 6.1 pixel⁻¹ (blue) and 11.8 pixel⁻¹ (red) were approached. Besides, there are also two spectra acquired for J1115+0544 from Keck and LAMOST (Yan et al. 2019). Details on the exposure time and slit selection for every single observation could be found in the Appendix A.

All spectra were reduced according to the standard reduction procedures for a long-slit spectrum. They were flux calibrated with the standard stars observed in the same night.

3. DATA ANALYSIS AND RESULTS

The main goal of this work is to identify the spectral features accompanying the MIR outburst by comparing the spectra taken before and after the MIR outburst, and their subsequent evolution. Although variations of prominent emission lines are obvious in many cases, a thorough analysis is essential to acquire robust detection and measurements of weak emission lines and for the entire sample.

3.1. Subtraction of the Continuum

Aiming at detecting potential characteristic emission-line variation, we began our analysis with subtraction of continuum. These spectra are first corrected for Galactic extinction using the extinction map of Schlegel et al. (1998) and the extinction curve of Fitzpatrick (1999).

Because the SDSS spectra are dominated by starlight, we fit them using the procedure PPXF (Cappellari & Emsellem 2004; Cappellari 2017) and MILES spectral library (Vazdekis et al. 2010). Nevertheless, the AGN continuum is likely not negligible for eight broad-line objects (§ 3.2), while the PPXF is a pure starlight component fitting code. So for these eight sources, we used the spectral decomposition results of Paper I instead. The fitting of J1647+3843 is shown as an example in Figure 1.

For the DBSP spectra observed after the MIR flare, an additional continuum component associated with the MIR outburst is possible. We thus also placed a reddened power-law continuum assuming an extinction curve of the Galactic dust (Fitzpatrick 1999), as normally appears in broad-line AGNs, in the fitting. On the other hand, the shape of the starlight component remains exactly the same as that of the SDSS

spectrum. Accordingly, we fit the continuum of DBSP spectra using the following formula:

$$A * S(\lambda) + B * \lambda^{\alpha} * 10^{-0.4 * E(B-V) * k(\lambda)} \quad (1)$$

$S(\lambda)$ is the starlight component of the same source obtained by applying the PPXF procedure to the SDSS spectrum, and the power-law index α was set to be in the range between -2 and -1. The $k(\lambda)$ is the extinction curve and $E(B-V)$ varies from 0 to 2.5.

The fitting was done by Python code MPFIT¹ and the errors of the parameters were estimated from Monte Carlo simulations. We show an example in the bottom panel of Figure 1.

3.2. Emission-line Fitting and Detection Criteria

After subtracting the continuum, the emission-line spectrum is modeled with a combination of Gaussian functions in several segments to measure the line fluxes of various broad and narrow lines. The broad lines include H α , H β , He II and Bowen line N III. The narrow lines contain [O III], [N II], [S II], [Ne III]. Each narrow line is modeled with one or two Gaussians, while broad H α and H β are fitted simultaneously with Gaussians of the same width and centroid in velocity. The number of Gaussians is determined according to the 95% threshold of improvement with the F-test by adding one more Gaussian to the fit. We show an example of H α and H β fitting results in the Figure 2.

However, a reliable detection of broad H α requires not only at least one broad component as suggested by the F-test but a 5 σ criterion was also demanded. Accordingly, eight sources in our sample have reliable broad H α detection in the SDSS spectra, which are taken before the MIR flare (see appendix A). For DBSP spectra, usually with multiple epochs, we have fitted and tried to detect broad H α in each of them. If there is no broad component detected in H α , we take the flux at the 90% confidence level as the upper limit which is derived from $\Delta\chi^2 = 2.7$ (Avni 1976). We will adopt broad H α , which is usually the strongest, if exists, to represent the evolution of broad components.

We consider seven common coronal lines, namely [Fe VII] λ 3759, [Fe V] λ 4071, [Fe XIV] λ 5304, [Fe VII] λ 5722, [Fe VII] λ 6087, [Fe X] λ 6376 and [Fe XI] λ 7894. Each is fitted with one Gaussian of FWHM < 1500 km s⁻¹ while a linear function has also been added to represent the local residual continuum (see Figure 2 for an example). An F-test is employed to assess whether the Gaussian component is necessary or not. A line is detected if its flux is above the 3 σ level. The presence of coronal lines is defined as the detection of three coronal lines or two lines with one above the 5 σ level

¹ <http://code.google.com/p/astrolibpy/source/browse/trunk/>

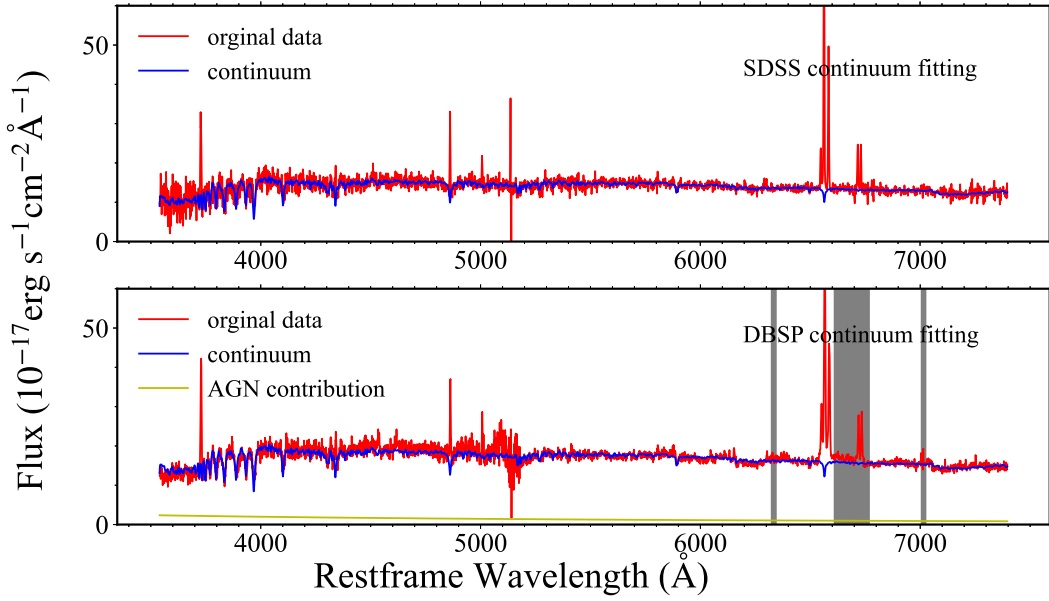


Figure 1. We show the continuum fitting of the spectrum of J1647+3843 before (SDSS, top panel) and after (DBSP, bottom panel) an MIR outburst as an example. The original SDSS spectrum is plotted in red and the fitted stellar continuum is shown in blue. For the DBSP spectrum taken after the outburst, an additional reddened power-law component (yellow) has been also included in the fitting. The shadow regions show the prominent telluric absorption windows, which were masked in the fitting procedure.

in the same epoch, or a coronal line in multiple epochs. According to the above rule, no coronal lines were present in all our SDSS spectra but they show up in the post-outburst spectra of nine objects.

3.3. Emission-Line Variations

Next we begin to check the emission-line variability between DBSP and SDSS spectra. Obviously, if broad $H\alpha$ is reliably detected in the SDSS spectrum, one has to measure the line flux to assess whether it is variable or not. This requires a reliable flux calibration. Although our spectra were already flux calibrated using a standard star, due to changes in weather conditions over the night, significant uncertainty could be introduced. With a reliable broad $H\alpha$ indicating significant nuclei activity, recalibration was done based on the normalization of the $[O III]\lambda 5007$ flux, which is assumed to be constant for the Seyfert galaxy over the monitoring timescale (Peterson et al. 2013). The variability of broad $H\alpha$ then was acquired by checking whether its flux at any epoch during the follow-up observations has changed by 3σ relative to the SDSS one or not. However, recalibration could not be implemented for J2215-0107, one of the eight sources with reliable broad $H\alpha$ detection in SDSS spectra, due to the too-low spectra quality, and we just removed it without further discussion (hence, 53 left). Significant variation of broad $H\alpha$ was found in the left seven. Counting those with newly emerged broad $H\alpha$, 22 in our samples display vari-

ation of broad $H\alpha$ and the appearance of coronal lines was in 9 of them. According to whether or not the variability of $H\alpha_{\alpha,B}$ or coronal lines is detected, our sample can be classified into three subclass (see Table 1). It is interesting to note that there is no object in our sample that shows only variation in coronal lines.

Additionally, as the $[O III]\lambda 5007$ flux of the seven with reliable broad $H\alpha$ in SDSS spectra and other Seyfert 2 galaxies was expected to be constant in our multiple DBSP follow-up spectra and the same as that of SDSS, the scatter of the $[O III]\lambda 5007$ flux normalized by the SDSS ones could thus be used to estimate the accuracy of the original flux calibration. The median value of the scatter is about 0.17 dex. When we focused on the long-term evolution (see Section 3.3.2), such uncertainty would be taken into consideration for MIRONG starting from normal galaxies without a reliable broad $H\alpha$ detection in SDSS and only when the variation amplitude exceeds 0.17 dex do we think there is an upward or downward trend.

3.3.1. The Variability in Different Galaxy Types

First, the percentage of objects that display emission-line variability differs greatly in different spectral types (see Table 1). It is remarkable yet not surprising to note that Seyfert galaxies possess the highest fraction given that AGNs display ubiquitous variability in both continuum and emission lines. In particular, all four Seyfert 1 galaxies show obvious

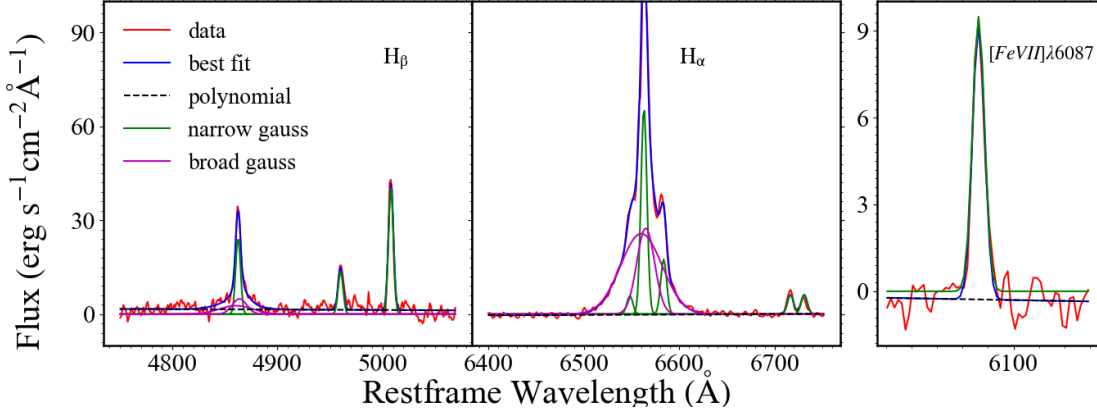


Figure 2. The left, middle, and right panel show the $H\beta$, $H\alpha$, and $[\text{Fe VII}]\lambda 6087$ fitting results respectively. The red curves in the three panels represent the original emission lines data while the blue curves represent the best-fitting model. Narrow and broad components are displayed with green and purple curves. The black dashed line models the residual local continuum, and only a few spectra's $H\alpha$ and $H\beta$ fitting need this component as shown in the figure to improve the fitting.

Table 1. Summary of Emission-line Variability

Class	Number	$H\alpha_{,B}$	$H\alpha_{,B}\text{-CL}$	None	Percentage
(1)	(2)	(3)	(4)	(5)	(6)
Starforming	15	4	1	10	33.3%
Composite	20	3	4	12	35.0%
Seyfert 1	4	2	2	0	100%
Seyfert 2	5	2	1	2	60.0%
LINER	9	2	1	6	33.3%
Total	53	13	9	31	41.5%

NOTE— The spectroscopically observed sample has been classified into three types (columns 3-5) based on the variability of broad $H\alpha$ and coronal lines, noting that there is none with only coronal line variability. Column (1): BPT class from SDSS spectra, which was collected from Paper I. Column (2): the number of objects in each class. Column (3): the number of objects with variations in broad $H\alpha$ but not coronal lines. Column (4): the number of objects with variations in both broad $H\alpha$ and coronal lines. Column (5): the number of objects with neither broad $H\alpha$ nor coronal line variations. Column (6): the percentage of sources that show emission-line variability ($H\alpha_{,B}$ or $H\alpha_{,B}\text{-CL}$) in the given class.

$H\alpha_{,B}$ variations, with coronal lines being detected in two of them. Though obvious variability is not expected for normal Seyfert 2 galaxies (e.g., Yip et al. 2009), the line variability found for the Seyfert 2 galaxies in our sample is understandable, because there is a high possibility for them to be changing-look AGNs considering the selection criteria. In contrast to Seyfert galaxies, the star-forming (SF) and composite galaxies present significantly lower portion of variability (33.3% and 35%, respectively), with the former dominated by $H\alpha_{,B}$ while the latter is dominated by $H\alpha_{,B}\text{-CL}$ variations. Low-ionization nuclear emission-line regions

(LINERs), which are usually considered to be photoionized by a weak AGN (Ferland & Netzer 1983; Halpern & Steiner 1983), hold the ratio same as star-forming galaxies though.

3.3.2. Long-term Evolution of Broad $H\alpha$ and Coronal Lines

All 22 objects with detection of emission-line variability with respect to SDSS spectra show an apparent increase in broad $H\alpha$ emission while only a small fraction of them show coronal-line variations. Except for J1442+5558 and J1003+0202, the strength of $H\alpha_{,B}$ declines again in the subsequent observations although most of them have not returned back to the flux level of SDSS as of the latest epoch. It indicates that the $H\alpha_{,B}$ emission fades slowly and a minority of them may sustain for a long time. Despite of their weakness, coronal lines clearly fade out after the first follow-up observation except for J1442+5558, whose coronal lines have just emerged in recent DBSP spectra while $H\alpha_{,B}$ has been detected in the first DBSP. We show the spectral evolution of J1442+5558 in Figure 3, and all 22 sources with emission line variation in Appendix B.

3.3.3. $\text{N III } \lambda 4686$ and $\text{He II } \lambda 4686$

During our spectroscopic analysis, we have noticed that some of them also show variations of $\text{He II } \lambda 4686$ and Bowen line $\text{N III } \lambda 4640$ apart from broad Balmer lines and iron coronal lines. Particularly, 7 of the 10 $H\alpha_{,B}\text{-CL}$ sources present $\text{He II } \lambda 4686$, with two of them (J1442+5558 and J1513+3111) even with $\text{N III } \lambda 4640$ emission. Both $\text{He II } \lambda 4686$ and $\text{N III } \lambda 4640$ lines are frequently detected in TDEs (van Velzen et al. 2021a).

3.4. Sources without a Visible Spectral Change

Among the 53 useful sources, 22 show obvious emission variability in at least broad $H\alpha$, while the other 31 appear unchanged in optical spectra according to our observations. It is necessary to explore whether the nondetection is intrinsic or

Table 2. *Summary of sources with emission-line variations*

Name	BPT	Time Coverage	$H_{\alpha,B}$ Behavior	Iron CLs	He II $\lambda 4686$	N III $\lambda 4640$	Interpretation
(1)	(2)	(3)	(4)	(5)	(6)	(7)	(8)
J0205+0004	SF	2017-2021	Restored	×	×	×	TDE
J0859+0922	SF	2018-2021	Declining	×	×	×	TDE
J1549+3327	SF	2017-2020	Restored	✓	✓	×	TDE
J1620+2407	SF	2019-2021	Declining	×	×	×	TDE
J1647+3843	SF	2018-2021	Declining	×	×	×	TDE
J1043+2716	Composite	2017-2021	Declining	✓	×	×	TDE
J1111+5923	Composite	2018-2020	Declining	×	×	×	TDE
J1442+5558	Composite	2017-2021	Maintain	✓	✓	✓	Turn-on
J1513+3111	Composite	2017-2021	Declining	✓	✓	✓	TDE
J2203+1124	Composite	2017-2019	Declining	✓	✓	×	TDE
J1315+0727	Composite(b)	2017-2017	Rising	×	×	×	AGN Flare ³
J1332+2036	Composite(b)	2017-2021	Declining	×	×	×	AGN Flare
J1133+6701	LINER(b)	2018-2021	Restored	×	×	×	AGN Flare
J1115+0544	LINER	2016-2021	Restored	✓	×	×	TDE
J1632+4416	LINER	2017-2018	Restored	×	×	×	TDE
J1003+0202	Seyfert 2	2018-2021	Maintain	×	×	×	Turn-on
J1238+0815	Seyfert 2	2017-2017	Declining	×	×	×	AGN Flare
J1657+2345	Seyfert 2	2017-2021	Declining	✓	✓	×	TDE
J0120-0829	Seyfert 1(b)	2017-2018	Restored ²	×	×	×	AGN Flare
J1105+5941	Seyfert 1(b)	2017-2021	Declining	✓	✓	×	TDE
J1402+3922	Seyfert 1(b)	2017-2021	Restored ¹	✓	✓	×	TDE
J1537+5814	Seyfert 1(b)	2017-2021	Restored ¹	×	×	×	AGN Flare

NOTE—This is a summary table of the 22 sources with emission-line variation. Column (2): BPT class from SDSS spectra. The galaxy types followed by a “b” in parentheses indicate that apparent broad Balmer lines were detected in their SDSS spectra according to the criteria in Section 3.2. Column (3): the first and last years of the follow-up observation. Column (4): all of the 22 sources show enhancement or emergence of broad $H\alpha$, but their subsequent $H_{\alpha,B}$ evolution behaviors are somewhat different, which could be generally divided into the following four types. (i) “Rising”: the $H_{\alpha,B}$ rises up continuously to the end of observations. (ii) “Declining”: the $H_{\alpha,B}$ apparently fades after enhancement but it is still at a level higher than in the SDSS spectra in the latest observation. (iii) “Restored”: the $H_{\alpha,B}$ shows a declining trend after the enhancement and it has almost returned back to the same level as SDSS now; (iv) “Maintain”, the $H_{\alpha,B}$ stays at a high level without a notable declining trend after the enhancement. Column (5): “✓” means iron coronal lines were detected in the DBSP spectra while “×” means not. Column (6): same as column (5) but gives the detection of He II $\lambda 4686$. Column (7): detection of N III $\lambda 4640$ or not. Column (8): preliminary interpretation of the MIRONG based on the spectral evolution.

¹The $H_{\alpha,B}$ in the two Seyfert I galaxies returned to the pre-outburst level about 1 yr after the first spectroscopic follow-up, continued to fade out and almost disappeared completely in the last epoch.

²The $H_{\alpha,B}$ had already declined to a level lower than in the SDSS spectrum after 5 months since brightening at the first epoch, yet it shows a rising trend again later, that is consistent with rebrightening in the MIR.

³“AGN flare” means we stopped at the result that these MIRONG were caused by AGN activity, without further preference for detailed physical processes behind (see 4.3)

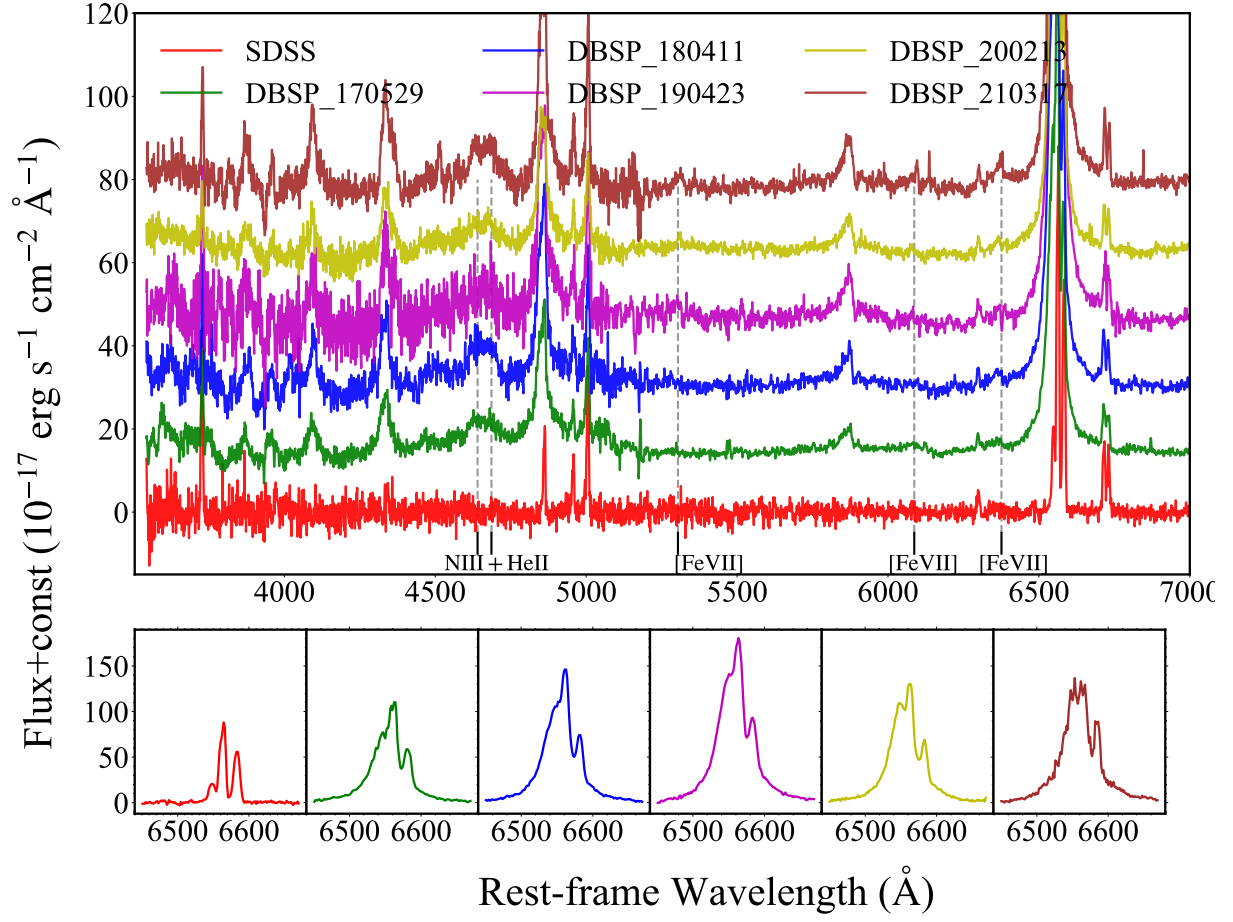


Figure 3. We show the spectral evolution of J1442+5558, including the whole spectral evolution (top panel, continuum subtracted) and the evolution of the H α region (bottom panel)

simply caused by selection effects. First, we have examined the S/N of the spectroscopic data of the variable and nonvariable subsamples as the higher-quality data are undoubtedly more helpful for the detection of weak emission lines embedded in the continuum. However, no obvious difference is found.

As we have shown in section 3.3.2, the $H\alpha_{,B}$ and iron coronal lines of most objects show apparent decreasing trends after brightening. Some of them have even disappeared rapidly, demanding quick spectral follow-ups to capture the variations. For this reason, if the spectroscopic observations were conducted too late, we might miss the fleeting emissions. We have calculated the time separation between the spectroscopic observational date and the first MIR brightening epoch (3σ brightening in either the W1 or W2 band; see details in Paper I). There is no significant difference between the spectral variable and nonvariable subclass according to a Kolmogorov–Smirnov (K-S) test. It seems that the non-detection of spectral variability should not be a consequence of too-late observations if the two subclasses share comparable decay timescales.

Dust is ubiquitous in galaxies from galactic disks to galactic centers. It is especially considerable for our MIRONG sample because they were selected by IR echoes radiated by the circumnuclear dust around SMBHs. The dust along the light of sight can obscure the optical photons, making them undetectable in both continuum and emission lines. Figure 4 shows the W1 band variability amplitude $\Delta W1$, W1 peak luminosity L_{W1} , dust temperature T_{dust} (data drawn from Paper I, also a significant difference in $\Delta W2$ and L_{W2}). All three parameters show a significant difference between the variable and nonvariable subclass based on a K-S test with the p -value being 3.1×10^{-5} , 1.1×10^{-5} , and 3.8×10^{-6} , respectively. In detail, the nonvariable sources have lower $\Delta W1$, L_{W1} and T_{dust} , which can be explained by the self-obscuration of dust emission. We have checked the narrow-line Balmer decrements of the two populations and found no difference, indicating a similarity in galactic-scale dust. The dust discrepancy between them might be in the galactic nucleus.

We have also looked into the distributions of other parameters, including M_{BH} and the rising and decay timescales of MIR light curves. All show negligible differences.

4. DISCUSSION

Optical spectra usually carry vital information for deciphering the nature of unknown transients. Aiming to explore the nature of the MIRONG sample, we have conducted extensive follow-up observations. Prominent emission-line variability has been detected in 22 out of the 53 objects (see details in Table 2). By means of the spectral results, we will show that the SN scenario is further proved to be the less likely case, corroborating the associations with SMBHs as

proposed in paper I. Specifically, we will try to understand the MIR outburst under the context of diverse transient accretion events of SMBHs, such as TDEs, turn-on AGNs, or sporadic gas accretion. Even for those without a visible spectral change, some clues can also be acquired.

4.1. SN Scenario Is Further Disfavored

In fact, the SN scenario has been largely excluded (paper I) based on MIRONG’s high MIR luminosity (see also Wang et al. 2018a) and their proximity to the galaxy center. Spectroscopic evolution further supports this conclusion.

First, the varying components in the optical spectra overwhelmingly feature emission but without notable absorption lines that are atypical for conventional SNe (Filippenko 1997). Further, the broad $H\alpha$ lasts typically 2–4 yr or more from their first detection in our sample, which is also in sharp contrast with the fast decline for a typical Type II SN (e.g., Uomoto & Kirshner 1986; Sahu et al. 2006). Only a subclass of SNe (Type IIn), which shows the signatures of the interaction between the SN ejecta and the circumstellar medium and exhibits obvious Balmer emissions, most notably $H\alpha$, with a weak or absent broad absorption component (Schlegel 1990; Filippenko 1997), bears some similarities with our sample. And some objects, such as SN2010jl (Fransson et al. 2014; Moriya et al. 2020), SN2015da (Tartaglia et al. 2020), SN2005ip (Stritzinger et al. 2012; Fox et al. 2020), and SN2006jd (Stritzinger et al. 2012), displayed a long-lasting broad $H\alpha$ with similar line luminosity to our sample and could be accompanied by coronal lines. However, their late-time spectra usually show prominent low-ionization emission lines such as near-infrared Ca II triplets and O I $\lambda 8446$, which are completely absent in our spectra. Hence, our spectroscopic results argue against an SN origin.

4.2. MIRONG Occurring in Normal or Weak-AGN Galaxies

The final sample of the 22 spectroscopically variable sources consists of 7 Seyfert galaxies according to their SDSS BPT classification. In addition, we note that there are three more galaxies in other classes, that is J1315+0727, J1332+2036 (composite), and J1133+6701 (LINER), that show evident broad $H\alpha$ in their SDSS spectrum. Therefore, we grouped the 10 sources (Seyferts or with a broad-line) into a subsample of unambiguous AGNs before the MIR outburst and the remaining 12 into a subsample without or with very weak AGNs. We begin our discussion with the latter subsample.

4.2.1. One Bona Fide Turn-on AGN Candidate

The sudden and drastic brightening in the centers of normal galaxies is usually attributed to TDEs or turn-on AGNs once the SN scenario is ruled out. Although in the literature the term ‘turn-on AGN’ was also used by some authors to

refer to changing-look AGN which transits from Seyfert 2 or 1.8 to type 1.5 or 1 (e.g., MacLeod et al. 2016; Yang et al. 2018; Wang et al. 2018b), we will strictly use the term to mean the transition from normal galaxies to Seyfert 1 galaxies or quasars. Gezari et al. (2017) reported the first case of a turn-on quasar, which transits from an absorption-line galaxy to a quasar in a surprisingly short time scale of a few months. Yan et al. (2019) presented a case of a transit from a LINER to a Seyfert 1 galaxy within a few years in SDSS 1115 discovered in the spectroscopic follow-up of the MIRONG sample. Both of these objects showed a plateau in the optical light curve following an initial brightening. Note that both objects displayed also strong IR echoes and are included in the MIRONG sample. Subsequently, six more transients from LINERs to broad-lined AGN-like spectra were discovered by ZTF (Frederick et al. 2019). Note that three of them also displayed weak broad emission lines in their pre-outburst spectra, which is similar to J1133+6701 in our sample. Nevertheless, most sources fade out in about a year, but with some fluctuations (Frederick et al. 2019, see Figure 5), different from those of known optical TDEs. Together with large black hole masses, which are derived from the correlations between M_{BH} and galactic properties, they appear more likely to be associated with nuclear activity than with TDEs, although the nature of these sources remains to be unraveled.

However, as we have mentioned above, the appearing broad $H\alpha$ in most objects fades immediately in the subsequent observations, indicating a short-lived accretion. Only J1442+5558 enters a long plateau phase in the light curve of $H\alpha_{,B}$, which has lasted for at least four years, and thus is a good candidate of a bona fide turn-on AGN. However, the integrated radiative energy to now for J1442+5558 is 1.1×10^{52} erg, well within the range expected for TDEs. Thus, further monitoring was also necessary to determine whether the $H\alpha_{,B}$ continues to stay at the high state or is going to decrease soon. In fact, J1115+0544, another object in our sample, has been thought of as a reliable bona fide turn-on AGN because its $H\alpha_{,B}$ has steadily been there for at least two years (2016-2018; Yan et al. 2019). However, the latest observation performed at UT 2021-01-07 shows that its $H\alpha_{,B}$ has almost disappeared, to our surprise.

4.2.2. Most are Good TDE Candidates

Therefore, the bona fide turn-on AGNs should be minorities in our sample since only one shows persistent $H\alpha_{,B}$ emission after the appearance. The remaining 11 are formally consistent with TDE-like transients. In particular, the $H\alpha_{,B}$ of J0205+0004, J1549+3327, and J1632+2345 has vanished rapidly within one year and J1115+0544 has also returned back to the flux level of SDSS though the strong broad $H\alpha$ has remained for at least 2 yr. Further monitoring of the other seven objects in the declining phase will inform us whether

their $H\alpha_{,B}$ would also fade away completely. We need to emphasize that the behavior of the $H\alpha_{,B}$ evolution is certainly not sufficient for concluding the nature of MIRONG although it can reflect the energy and timescale of the primary emission to some extent. Actually, our knowledge of the spectral characteristics accompanied by various SMBH transients is still in the accumulation stage and awaiting in-depth understanding.

Besides the above-mentioned $H\alpha_{,B}$ emission, it is notable that iron coronal lines have been detected in 5 of the 11 sources, with 3 also being detected with $\text{He II } \lambda 4686$ and 1 being detected with $\text{N III } \lambda 4640$. All of these emission lines are previously found and used to claim a TDE. Remarkably, the ZTF group has recently classified their uniformly selected TDE sample into three categories based on whether or not the hydrogen Balmer lines, $\text{He II } \lambda 4686$ and $\text{N III } \lambda 4640$ are present (van Velzen et al. 2021a), although the physics that drives the diversity is still poorly understood. Aside from the TDEs found by optical photometric surveys, the spectroscopic selection by extreme iron coronal lines in normal galaxies has also been proven to be a valid approach (Komossa et al. 2008; Wang et al. 2011, 2012), theoretically supported by the anticipation that TDEs can nicely provide the soft X-ray-ionizing photons. Their transient nature has been further confirmed by the long-term spectral evolution (Yang et al. 2013), dust IR echoes (Dou et al. 2016), and soft X-ray radiation (He et al. 2021). In terms of the similarity of prominent IR echoes and high detection rate of coronal lines, our sample could be most likely to be analogous to the coronal-line selected TDEs.

In brief, the appearance and fading of $H\alpha_{,B}$, iron coronal lines, $\text{He II } \lambda 4686$ and $\text{N III } \lambda 4640$ are all nice evidence for TDEs although the real benchmark of the TDE spectrum is still poorly known.

4.2.3. The Possibility of Sporadic Gas Accretion

Our MIRONG sample is very different from optical TDEs in IR echoes. A systematic investigation of the MIR light curves of optical TDEs suggest that their echoes are very weak or negligible, yielding a very low dust-covering factor (f_c) of those SMBHs (Jiang et al. 2021b; van Velzen et al. 2016, 2021b). On the contrary, the high MIR luminosity of MIRONG definitely gives a much higher f_c (Jiang et al. 2021a). The locally gas-rich environment means that the SMBH will not likely starve due to lack of gas supply permanently. Is it possible that the sporadic gas accretion or instability in the accretion flow triggers the transient accretion?

First, the instability of the gas reservoir in the outer disk may result in sporadic feeding to the central black hole. Such a process is invoked to explain changing-look AGNs. Radiation pressure instability in the inner accretion disk with a very

low accretion rate is exceedingly longer than the observed timescale (Gezari et al. 2017). While standard limit-cycle instability, as in cataclysmic variables, in the outer disk can be ruled out because of its very long timescale (Lin & Shields 1986), a modified version of the limit-cycle instability model was proposed for changing-look AGNs (Sniegowska et al. 2020). In the quiescent state, the accretion rate is low, and the system consists of a truncated outer thin disk and an inner hot advection-dominated flow. The instability takes place in a narrow ring of the thin disk on the boundary of two accretion flows at a few tens of the Schwarzschild radius. Although the model is still under development, initial analysis of the stability of a narrow ring does suggest it is able to reproduce the short transit timescale of months to years observed in changing-look AGN as well as in our objects. The duty cycle increases with increasing steady accretion rate, viscosity, and width of the ring. A low steady accretion rate, and thus low duty cycle, may explain the lack of a prominent AGN signature in the narrow-line spectra, although further detailed modeling is required to confirm this.

Second, stochastic feeding by a cold gas cloud, such as G1/2 clouds in the Galactic center, may eventually lead to an outburst. The presence of thick dust components on subparsec to parsec scales as revealed by IR echoes indicates the presence of a rich cold gas environment, analogously with a circumnuclear molecular disk at the Galactic center, in which the G2 cloud originated (Schartmann et al. 2015). Although the encounter of G2 with the supermassive black hole did not significantly increase the accretion rate from both observations and numerical simulations (Morsony et al. 2017), strong mass feeding may be expected if a dense thin disk is present. In that case, the collision between the cloud and dense gas in the disk may result in significant dissipation, likely ending in gas accretion. For a high plunged cloud, tidal disruption will further increase the cross section of collision, enhancing such fueling process. However, as the encounter of a cloud takes place at $10^2 - 10^3 r_s$, and the accretion time is expected long if the disk remains cold. Nevertheless, the encounters with clouds are random. If the directions of angular momentum of the disk and the cloud are opposite, the collision may leave a significant fraction of very low-angular-momentum gas, which can be quickly accreted.

4.3. *MIRONG Occurring in AGNs*

The real physics behind MIRONG in active galaxies could be complicated and diverse, with turn-on AGNs, unusual AGN variability, and TDEs all possible. Distinguishing between them is quite challenging to our current knowledge. We will try to give our initial impression of them here, leaving a detailed analysis to our subsequent works.

The amplitude of stochastic variability, which is a defining characteristic of AGNs, is generally not higher than

tenths of a magnitude within months to years although it increases toward longer timescales (e.g., Vanden Berk et al. 2004; MacLeod et al. 2010). Only the most extreme tail of AGN variability distribution may show an amplitude comparable with TDEs over a short period of time (e.g., MacLeod et al. 2012; Rumbaugh et al. 2018). Moreover, conventional AGN variability does not show regular and smooth patterns, such as the power-law decay seen in TDEs. Nevertheless, there indeed exists a population of AGNs displaying major flares at timescales of years, which resembles TDEs more, in their light curves, (e.g., Graham et al. 2017; Kankare et al. 2017; Trakhtenbrot et al. 2019). The nature of these AGN flares remains very elusive even with spectroscopic observations as we still lack adequate information to distinguish each scheme from impostors at the benchmark level (Zabludoff et al. 2021), as we emphasized in the last section.

Exploration of our MIRONG sample becomes even difficult without direct variability information of their original emission. Luckily, emission-line variability, which can be considered as an alternative tracer, has been detected in most objects (see Table 1). The detection of $H\alpha_{,B}$ variation itself is not a surprise for AGNs, yet their rapid evolution may shed light on the central ionizing sources. Characteristic emissions other than $H\alpha_{,B}$, namely iron coronal lines and $HeII\lambda 4686$, might give further clues to the outburst. Only three objects (J1105+5941, J1402+3922, and J1657+2345) show these emissions, and their $H\alpha_{,B}$ has either been restored or is steadily declining. We thus take the three as tentative TDEs in AGNs for the time being as both iron coronal and $HeII\lambda 4686$ are representative features of TDE spectra, although not decisive.

For the remaining sources, only $H\alpha_{,B}$ variability has been found and their physics are even harder to constrain. To be consistent with prior definitions, we categorize J1003+0202, which was a Seyfert 2 and presented stable $H\alpha_{,B}$ after the brightening, as a turn-on subclass while the rest sources as AGN flares. We note that J1315+0727 only has two observations in 2017 and its $H\alpha_{,B}$ was still rising. More recent spectra will confirm whether it has faded away now. It should be emphasized again that the flares here may be caused by distinct processes in different sources, such as TDE, sporadic gas accretion, or special accretion disk instability.

4.4. *MIRONG without Spectral Variation*

The nature of the other 31 objects without clear spectral variations is still mysterious, yet might be even more fascinating. One possibility is that they belong to a new population of fast transients, which evolve much faster than variable sources. The high-cadence surveys over the past decade have indeed revealed a population of transients with timescales obviously shorter than those of SNe and TDEs, and are simply called "Rapidly Evolving Transients" or "Fast-Blue Optical

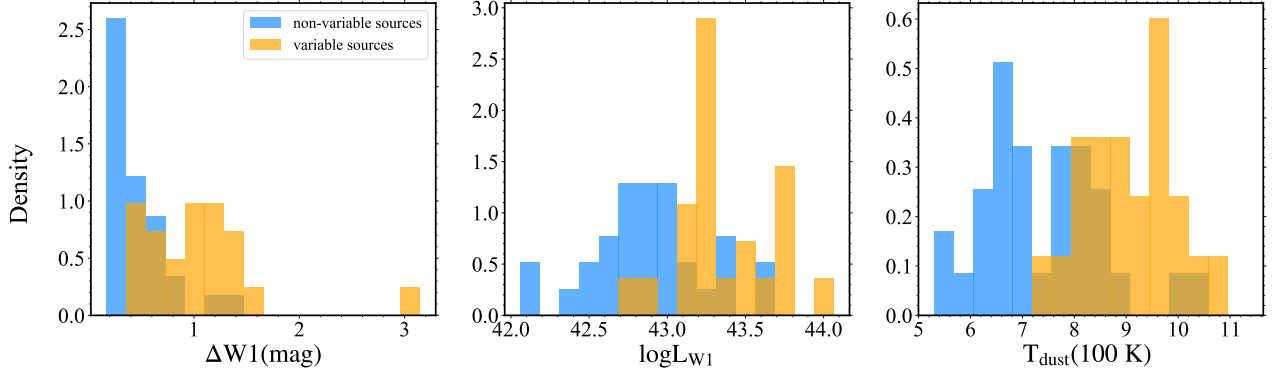


Figure 4. We show the comparison of the $W1$ -band variability amplitude $\Delta W1$ (left panel), logarithmic $W1$ peak luminosity $\log L_{W1}$ (middle panel), and dust temperature T_{dust} (right panel). All data were drawn from Paper I, in which the dust temperature was picked out from results fitting with dust absorption coefficient.

Transients" (FBOTs) in literature (e.g., Drout et al. 2014; Pursiainen et al. 2018) as their physical origin remains a puzzle. For instance, the nearest and most well-studied case, AT 2018cow, shows a rise-to-peak timescale of only three days and faded away within a couple of months (Margutti et al. 2019; Perley et al. 2019). The reprocessed MIR light curves cannot reflect the intrinsic outburst timescales unambiguously due to their coupling with dust distributions. Moreover, the optical surveys that overlapped with the outbursting period of our MIRONG sample have either poor cadence (e.g., PanSTARRS, PTF) or depth (e.g., ASASSN), thus they cannot put effective constraints on their optical emission. For likely the same reason, most of them have been missed by optical surveys. Future selection of more recent MIRONG, such as the outbursts after 2018 with both excellent WISE and ZTF light curves, may help test the fast transient hypothesis as the ZTF survey has a much higher cadence and depth compared with previous surveys.

The discrepancy in the dust properties (see Section 3.4) suggests that the dust obscuration may play a vital role and those spectral nonvariable sources correspond to more seriously obscured ones. In this scenario, they are good candidates of obscured TDEs, turn-on AGNs, or any other types of SMBH transients that are undetectable in optical bands. The discrepancy in IR emission can be also partly accounted for by the possibility that the outburst energy of the nonvariable sources is systematically lower than that of variable sources if their dust contents (covering factor) are identical. Further investigations with the aid of multiwavelength observations (e.g., radio; Mattila et al. 2018) are needed to make a conclusion about whether they are real dust-obscured events or an intrinsically distinct population.

5. CONCLUSIONS

As the first and essential step to identifying the nature of MIRONG, which are selected by a blind search, spectroscopic observations yield much valuable information of the

outbursts. The main results and conclusions are summarized as below.

1. We have obtained optical spectra for 54 objects (53 useful) in the MIRONG sample since 2017. Among them, 22 show the appearance or significant brightening of the broad $H\alpha$ ($H\alpha_{,B}$) emission, corroborating the primary conclusion drawn from Paper I, that is the MIR outbursts are mainly connected with dust echoes of transient SMBH accretion events. Regarding the difference types of galaxies, Seyferts have the highest ratio of $H\alpha_{,B}$ variability while a third of the other types (SF, composite, and LINER) also show an obvious change in $H\alpha_{,B}$.
2. Multiepoch spectroscopic observations have been continuously carried out for targets with the detection of $H\alpha_{,B}$ variability until the broad $H\alpha$ component has disappeared or been restored. Most of them display a declining trend immediately after the brightening, suggesting short-lived transients, such as TDEs, sporadic gas accretion, or special AGN variability. Only two show long-term stable $H\alpha_{,B}$ emission, which is more in agreement with the turn-on AGN scenario. Particularly, the composite galaxy J1442+5558 is an excellent candidate to be a bona fide turn-on AGN, which is hitherto extremely rarely found.
3. The characteristic iron coronal lines, $HeII\lambda 4686$ and $NIII\lambda 4640$ have also been detected in quite a fraction of these objects, which could provide further clues to their nature. We have naively classified the sources with multiple transient emissions as TDE candidates, particularly for those occurring in inactive galaxies. The real origin of outbursts in AGNs could be diverse and challenging to distinguish from each other as they still lack an accepted benchmark in spectra to our knowledge.

4. Sources without spectral variations do not behave differently in most distributions. The lower MIR luminosity and dust temperature of the nonvariable sources could be a result of self-obscuration although intrinsic weakness is also possible. If those objects are indeed more obscured TDEs, turn-on AGNs, or any other types of SMBH transients, they are worthy of further studies with the aid of observations from other bands (e.g., radio). Another explanation could be that they belong to a new population of fast transients yet without compelling evidence currently.

The nature of MIRONG has been further joined with SMBH transient accretion events based on spectral results while their specific physics remains ambiguous. Actually, the community is still vague as to how to distinguish between different types of nuclear transients accurately. A more detailed analysis of individual sources or subsets will be presented in our subsequent papers. Regardless of what is the true case eventually, MIRONG must be an indispensable part of mounting SMBH transient events, i.e., as a substantial supplement for the optical sample. The NEOWISE survey is still in commission and should yield out more MIRONG after our primary selection (Jiang et al. 2021a). The more recent MIRONG sample nicely meets the golden era of time-domain surveys at multiple wavelengths, such as ZTF (Bellm et al. 2019), LSST (Ivezić et al. 2019), and WFST in the optical band and eROSITA (Merloni et al. 2012) and the Einstein Probe (Yuan et al. 2015) in the X-ray band. We have the opportunity to perform a more comprehensive study with the new MIRONG sample and to move forward in understanding the mysterious events conclusively.

ACKNOWLEDGMENTS

We thank the referee for helpful comments and suggestions, which led to the improvement of the paper. This work is supported by the B-type Strategic Priority Program of the Chinese Academy of Sciences (Grant No. XDB41000000), Chinese Science Foundation (NSFC-11833007, 12073025, 11421303, 12103048, 11822301), China Manned Space Project (CMS-CSST-2021-B11) and the Fundamental Research Funds for the Central Universities. This research uses data obtained through the Telescope Access Program (TAP). Observations obtained with the Hale Telescope at Palomar Observatory were obtained as part of an agreement between the National Astronomical Observatories, Chinese Academy of Sciences, and the California Institute of Technology.

A. SUMMARY OF SPECTROSCOPIC FOLLOW-UP OBSERVATIONS

We show the spectroscopic follow-up observations and some basic information in the Table 3 at this appendix.

Table 3. Summary of spectroscopic follow-up observations

name	redshift	Type	telescope	observation date YYMMDD	exposure time s	slit width arcsec
SDSSJ010320.42+140149.8	0.0418	StarForming	P200	171216	1200	1.5
SDSSJ012047.99-082918.4	0.0347	Seyfert 1(b)	P200	170630	600	1.5
			P200	171124	1500	1
			P200	180105	1200	1
SDSSJ020552.16+000411.8	0.0765	StarForming	P200	171111	1200	1.5
			P200	171124	600	1
			P200	210107	900	1.5
SDSSJ081403.78+261144.3	0.0757	StarForming	P200	171026	1200	1.5
			P200	171124	900s	1
SDSSJ083536.49+493542.7	0.0424	Composite	P200	200213	1200	1.5
SDSSJ085959.46+092225.6	0.1519	StarForming	P200	180224	1800	1.5
			P200	200213	1800	1.5
			P200	210317	1800	1
SDSSJ090924.55+192004.8	0.1072	Composite	P200	170420	900	1.5
			P200	170529	900	1.5
			P200	171124	900	1
SDSSJ094303.26+595809.3	0.0749	LINER	P200	180224	1200	1.5
SDSSJ094456.56+310552.2	0.0346	Composite	P200	200213	1200	1.5
SDSSJ100350.97+020227.6	0.1247	Seyfert 2	Lick/Shane	180318	1200	1.5
			P200	190423	1200	1.5
			P200	200213	1200	2
			P200	210317	1800	1
SDSSJ103753.68+391249.6	0.1068	StarForming	P200	200213	1800	1.5
SDSSJ104306.56+271602.1	0.1281	Composite	P200	170420	900	1.5
			P200	170525	1560	1.5
			P200	171111	2100	1.5
			P200	171124	900	1
			P200	180224	1800	1.5+2.0
			P200	180411	1500	1
			P200	210317	1800	1
SDSSJ105801.52+544437.0	0.1306	StarForming	P200	200213	1200	1.5
SDSSJ110501.98+594103.5	0.0337	Seyfert 1(b)	P200	170525	900	1.5
			P200	171111	1200	1.5
			P200	171124	800	1
			P200	180224	1200	1.5
			P200	180411	800,700	1

Table 3 *continued*

Table 3 (*continued*)

name	redshift	Type	telescope	observation date YYMMDD	exposure time s	slit width arcsec
SDSSJ110958.34+370809.6	0.026	LINER	P200	200213	1200	2
			P200	210317	1200	1
			P200	170525	900	1.5
			P200	171124	600	1
SDSSJ111122.44+592334.3	0.1697	Composite	P200	210317	1200	1
			Lick/Shane	180318	1800	1.5
			P200	190423	1200	2
SDSSJ111536.57+054449.7	0.09	LINER	P200	200213	1200	1.5
			LAMOST	160106	5400	3 ^a
			P200	170525	1500	1.5
			P200	171111	1200	1.5
			P200	171124	1200	1
			P200	180114	1200	1.5
			P200	180408	1200	1.5
			P200	180411	1800	1
			Keck	180513	600	1
			P200	210107	1200	1.5
			P200	170525	1200	1.5
			P200	171124	900	1
SDSSJ112446.21+045525.4	0.074	Composite	P200	180224	1200	1
			P200	180408	1800	1.5
SDSSJ112916.12+513123.5	0.0329	Composite	P200	170529	900	1.5
			P200	171124	900	1
SDSSJ113355.93+670107.0	0.0397	LINER(b)	Lick/Shane	180511	1800	1.5
			P200	190423	1200	2
			P200	200213	1200	1.5
			P200	210317	1800	1
SDSSJ113901.27+613408.5	0.1346	StarForming	Lick/Shane	180318	1800	1.5
			P200	180408	1200	1.5
SDSSJ120338.31+585911.8	0.0469	StarForming	Lick/Shane	180612	1800	1
SDSSJ121907.89+051645.6	0.0825	Composite	Lick/Shane	180318	1200	1.5
SDSSJ123852.87+081512.0	0.1138	Seyfert 2	P200	170529	900	1.5
			P200	171124	600	1
SDSSJ124521.42-014735.4	0.2154	LINER	P200	180408	1200	1.5
SDSSJ130532.91+395337.9	0.0725	LINER	Lick/Shane	180318	1200	1.5
SDSSJ130815.57+042909.6	0.0483	Seyfert 2	P200	180224	600	1
SDSSJ131509.34+072737.6	0.0918	Composite(b)	P200	170529	900	1.5
			P200	171124	600	1
SDSSJ132259.94+330121.9	0.1269	LINER	P200	180408	1200	1.5
SDSSJ132902.05+234108.4	0.0717	Composite	Lick/Shane	180318	1800	1.5
			Lick/Shane	180613	1800	1.5

Table 3 *continued*

Table 3 (*continued*)

name	redshift	Type	telescope	observation date YYMMDD	exposure time s	slit width arcsec
SDSSJ133212.62+203637.9	0.1125	Composite(b)	P200	170622	600	1.5
			P200	171124	600	1
			P200	180411	800,850	1
			P200	190423	1200	2
			P200	190621	1200	1.5
			P200	210317	1200	1
SDSSJ140221.26+392212.3	0.0637	Seyfert 1(b)	P200	170622	600	1.5
			P200	171124	600	1
			P200	180408	1200	1.5
			P200	180411	1200	1
			Lick/Shane	180612	1800	1
			P200	200213	1800	1.5
SDSSJ140648.43+062834.8	0.0845	StarForming	P200	210107	1200	1.5
			P200	170525	1200	1.5
SDSSJ141235.89+411458.5	0.1025	Composite	P200	190423	1200	2
			P200	180408	1200	1.5
SDSSJ144227.57+555846.3	0.0769	Composite	P200	170529	900	1.5
			P200	180224	1200	1
			P200	180411	1200,1220	1
			P200	180607	1200	1
			P200	190423	1200	2
			P200	190621	1800	1.5
			P200	200213	1200	1
			P200	210317	1200	1
SDSSJ150844.22+260249.1	0.0826	Composite	Lick/Shane	180613	1800	1.5
SDSSJ151257.18+280937.5	0.1155	LINER	P200	180224	600	1
			Lick/Shane	180613	1800	1.5
SDSSJ151345.76+311125.0	0.0718	Composite	P200	170602	1500	1.5
			P200	180411	1200,1230	1
			P200	180607	1200	1
			P200	190423	1200	2
			P200	210317	1200	1
SDSSJ153711.29+581420.2	0.0936	Seyfert 1(b)	P200	170622	600	1.5
			P200	180411	1200,1230	1
			Lick/Shane	180612	1800	1
			P200	190621	1600	1.5
			P200	200213	1800	1.5
SDSSJ154955.19+332752.0	0.0857	StarForming	P200	210107	1500	1.5
			P200	170602	900	1.5
			P200	180411	1200,1230	1
			P200	180607	1200	1

Table 3 *continued*

Table 3 (*continued*)

name	redshift	Type	telescope	observation date YYMMDD	exposure time s	slit width arcsec
			P200	190423	1200	2
			P200	200213	1800	1.5
SDSSJ155437.26+525526.4	0.0664	Composite	Lick/Shane	180613	1800	1.5
SDSSJ155539.95+212005.7	0.0709	Composite	Lick/Shane	180318	1800	1.5
			Lick/Shane	180613	1800	1
SDSSJ155743.52+272753.0	0.0316	Composite	Lick/Shane	180318	1800	1.5
SDSSJ160052.26+461242.9	0.1974	StarForming	P200	190621	1200	1.5
SDSSJ162034.99+240726.5	0.0655	StarForming	P200	190621	1200	1.5
			P200	210317	900	1
SDSSJ162810.03+481047.7	0.1245	StarForming	Lick/Shane	180612	1800	1
SDSSJ163246.84+441618.5	0.0579	LINER	P200	170602	900	1.5
			Lick/Shane	180511	1800	1.5
SDSSJ164754.38+384342.0	0.0855	StarForming	Lick/Shane	180318	1800	1.5
			Lick/Shane	180612	1800	1
			P200	210317	1200	1
SDSSJ165726.81+234528.1	0.0591	Seyfert 2	P200	170602	900	1.5
			P200	180607	1200	1.5
			P200	190423	1800	1.5
			P200	190621	1800	1.5
			P200	210317	1800	1
SDSSJ165922.65+204947.4	0.0451	Seyfert 2	Lick/Shane	180318	1200	1.5
			Lick/Shane	180511	1800	1.5
SDSSJ214603.88+104128.6	0.1636	StarForming	P200	190621	1200	1.5
SDSSJ220349.23+112433.0	0.1863	Composite	P200	170628	1200	1.5
			P200	171111	2400	1.5
			P200	171124	1500	1
			Lick/Shane	180612	1800	1
			P200	190621	1200	1.5
SDSSJ221541.60-010721.0	0.0477	Composite(b)	Lick/Shane	180612	1200	1

NOTE—The host galaxy spectral type in the third column was collected from Paper I, and the galaxy types followed “b” in bracket indicated that apparent broad balmer lines were detected in their *SDSS* according to the criteria in 3.2. At the most time, the exposure time displayed in the sixth column was the same with each other for red and blue end observation ,but sometimes their may be a little difference, for which in the table the left one represented the blue end exposure time

^aThe 3'' given here for the LAMOST spectrum is the spectral fiber diameter.

B. SPECTRAL EVOLUTION OF THE 21 SOURCES WITH EMISSION LINES VARIATION

All 22 variable sources' spectral evolution are shown in Figure 5, 6, 7 in this appendix.

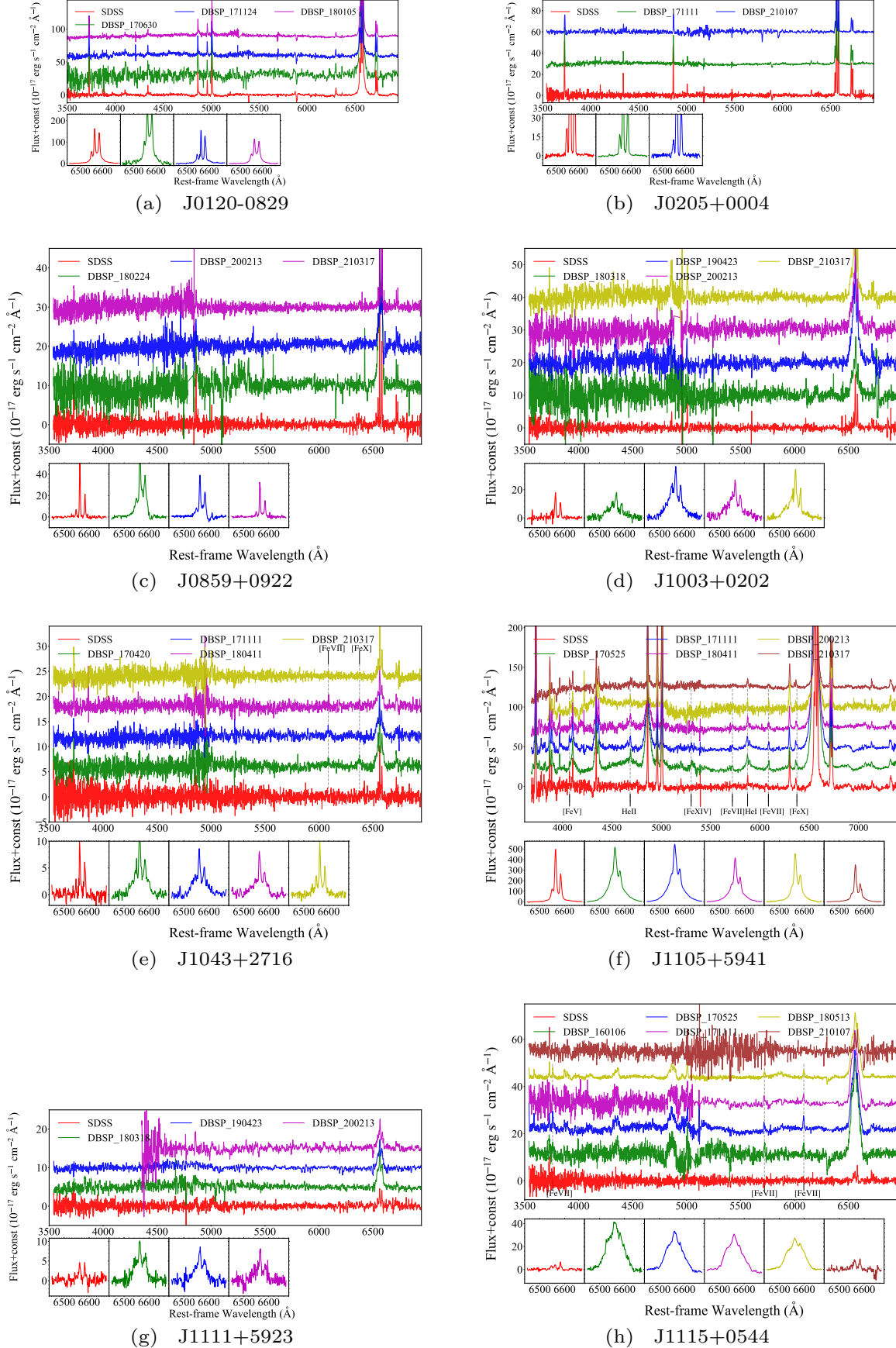


Figure 5. Spectral evolution of variable sources. For the source J1111+5923, the original flux calibration of Lick-180318 was not good, and we took the recalibrated one by making the narrow H α flux the same as that of DBSP-200213 because they have similar observation conditions.

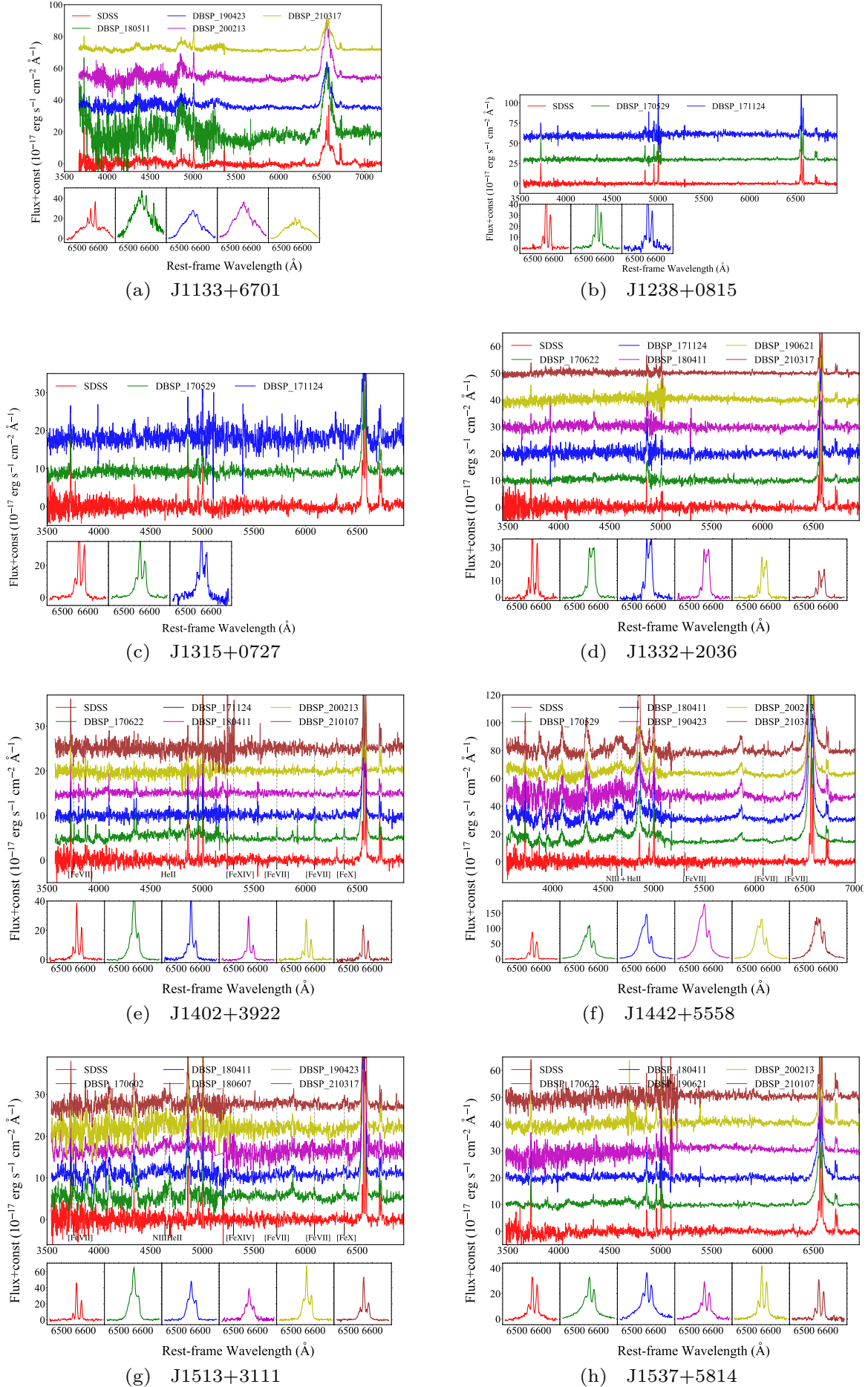
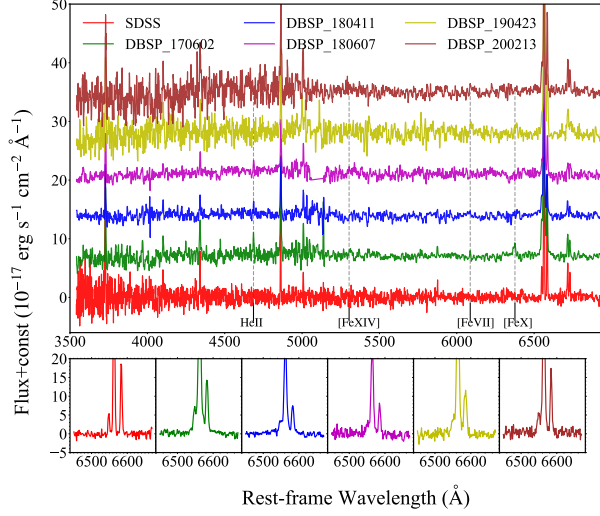
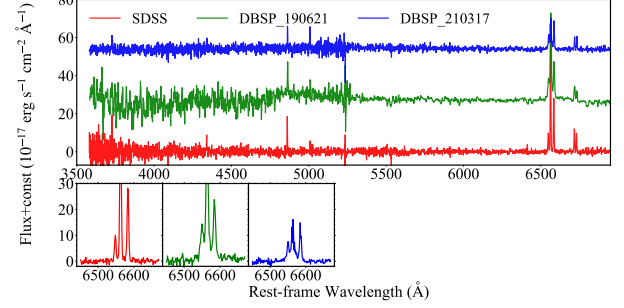


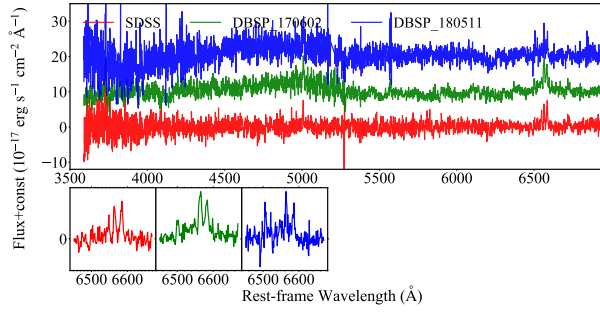
Figure 6. Spectral evolution of variable sources. For the source J1133+6701, the recalibration was not applied for DBSP_180511 because of the bad S/N of its [O III] λ 5007.



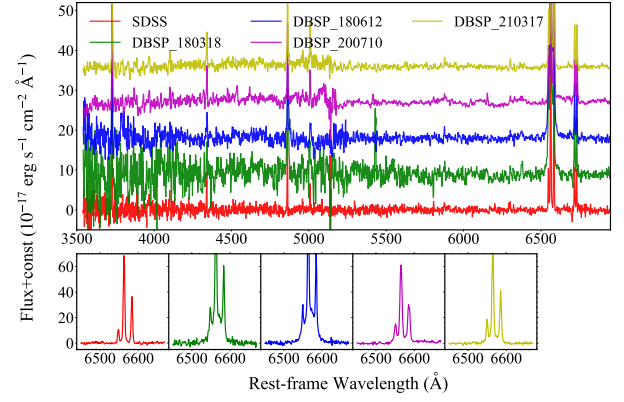
(a) J1549+3327



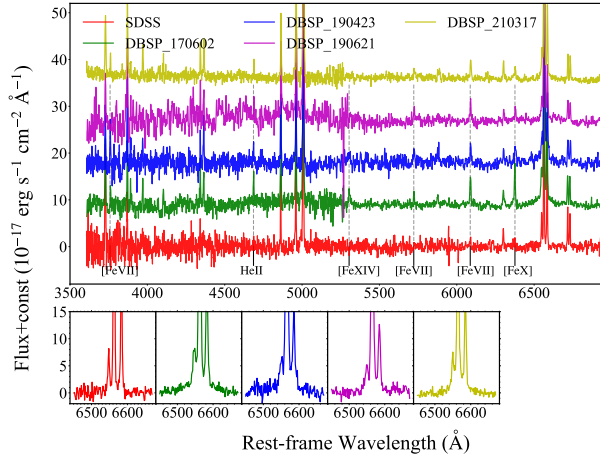
(b) J1620+2407



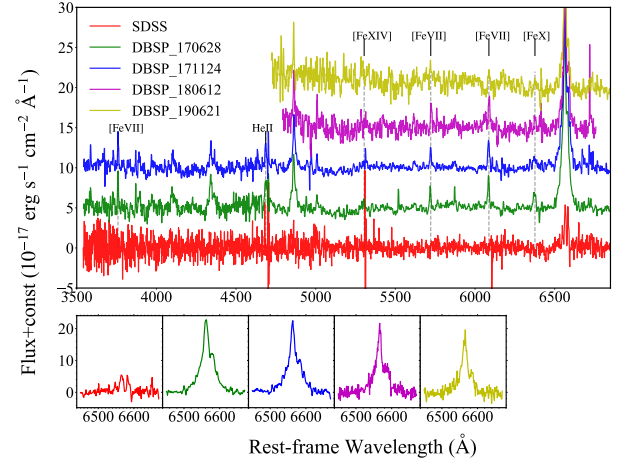
(c) J1632+4416



(d) J1647+3843



(e) J1657+2345



(f) J2203+1124

Figure 7. Spectral evolution of variable sources.

REFERENCES

- Avni, Y. 1976, *ApJ*, 210, 642
- Alexander, K. D., van Velzen, S., Horesh, A., et al. 2020, *SSRv*, 216, 81
- Bade, N., Komossa, S., & Dahlem, M. 1996, *A&A*, 309, L35
- Bellm, E. C., Kulkarni, S. R., Graham, M. J., et al. 2019, *PASP*, 131, 018002
- Bloom, J. S., Giannios, D., Metzger, B. D., et al. 2011, *Science*, 333, 203
- Burrows, D. N., Kennea, J. A., Ghisellini, G., et al. 2011, *Nature*, 476, 421
- Cappellari, M. 2017, *MNRAS*, 466, 798
- Cappellari, M. & Emsellem, E. 2004, *PASP*, 116, 138
- Dou, L., Wang, T., Jiang, N., et al. 2016, *ApJ*, 832, 188
- Drout, M. R., Chornock, R., Soderberg, A. M., et al. 2014, *ApJ*, 794, 23.
- Evans, C. R., & Kochanek, C. S. 1989, *ApJL*, 346, L13
- Ferland, G. J. & Netzer, H. 1983, *ApJ*, 264, 105.
- Filippenko, A. V. 1997, *ARA&A*, 35, 309
- Fitzpatrick, E. L. 1999, *PASP*, 111, 63
- Fox, O. D., Fransson, C., Smith, N., et al. 2020, *MNRAS*, 498, 517
- Fransson, C., Ergon, M., Challis, P. J., et al. 2014, *ApJ*, 797, 118
- Frederick, S., Gezari, S., Graham, M. J., et al. 2019, *ApJ*, 833, 31
- Gezari, S., Hung, T., Cenko, S. B., et al. 2017, *ApJ*, 835, 144
- Gezari, S. 2021, *arXiv:2104.14580*
- Graham, M. J., Djorgovski, S. G., Drake, A. J., et al. 2017, *MNRAS*, 470, 4112
- Guo, H., Sun, M., Liu, X., et al. 2019, *ApJL*, 883, L44
- Halpern, J. P. & Steiner, J. E. 1983, *ApJL*, 269, L37
- He, J. S., Dou, L. M., Ai, Y. L., et al. 2021, *A&A*, 652, A15
- Hinkle, J. T., Holoien, T. W.-S., Shappee, B. J., et al. 2021, *arXiv:2108.03245*
- Ivezić, Ž., Kahn, S. M., Tyson, J. A., et al. 2019, *ApJ*, 873, 111
- Jiang, N., Dou, L., Wang, T., et al. 2016, *ApJL*, 828, L14
- Jiang, N., Wang, T., Dou, L., et al. 2021a, *ApJS*, 252, 32
- Jiang, N., Wang, T., Hu, X., et al. 2021b, *ApJ*, 911, 31
- Kankare, E., Kotak, R., Mattila, S., et al. 2017, *Nature Astronomy*, 1, 865
- Komossa, S., Zhou, H., Wang, T., et al. 2008, *ApJL*, 678, L13
- Kool, E. C., Reynolds, T. M., Mattila, S., et al. 2020, *MNRAS*, 498, 2167
- Kormendy, J., & Ho, L. C. 2013, *ARA&A*, 51, 511
- LaMassa, S. M., Cales, S., Moran, E. C., et al. 2015, *ApJ*, 800, 144
- Lin, D. N. C. & Shields, G. A. 1986, *ApJ*, 305, 28
- Lu, W., Kumar, P., & Evans, N. J. 2016, *MNRAS*, 458, 575
- Lu, W., Kumar, P., & Narayan, R. 2017, *MNRAS*, 468, 910
- MacLeod, C. L., Ivezić, Ž., Kochanek, C. S., et al. 2010, *ApJ*, 721, 1014
- MacLeod, C. L., Ivezić, Ž., Sesar, B., et al. 2012, *ApJ*, 753, 106
- MacLeod, C. L., Ross, N. P., Lawrence, A., et al. 2016, *MNRAS*, 457, 389
- Malyali, A., Rau, A., Merloni, A., et al. 2021, *A&A*, 647, A9
- Margutti, R., Metzger, B. D., Chornock, R., et al. 2019, *ApJ*, 872, 18
- Merloni, A., Predehl, P., Becker, W., et al. 2012, *arXiv:1209.3114*
- Miller, J. S., & Stone, R. P. S., 1993, *Lick Obs. Tech. Rep.*, No. 66
- Moriya, T. J., Stritzinger, M. D., Taddia, F., et al. 2020, *A&A*, 641, A148
- Morsony, B. J., Gracey, B. T., Workman, J. C., et al. 2017, *ApJ*, 843, 29
- Mattila, S., Pérez-Torres, M., Efstathiou, A., et al. 2018, *Science*, 361, 482
- Mockler, B., Guillochon, J., & Ramirez-Ruiz, E. 2019, *ApJ*, 872, 151
- Oke, J. B. & Gunn, J. E. 1982, *PASP*, 94, 586
- Pasham, D. R., Remillard, R. A., Fragile, P. C., et al. 2019, *Science*, 363, 531
- Perley, D. A., Mazzali, P. A., Yan, L., et al. 2019, *MNRAS*, 484, 1031
- Peterson, B. M., Denney, K. D., De Rosa, G., et al. 2013, *ApJ*, 779, 109
- Phinney, E. S. 1989, *The Center of the Galaxy*, 136, 543
- Pursiainen, M., Childress, M., Smith, M., et al. 2018, *MNRAS*, 481, 894.
- Rees, M. J. 1988, *Nature*, 333, 523
- Rumbaugh, N., Shen, Y., Morganson, E., et al. 2018, *ApJ*, 854, 160
- Runnoe, J. C., Cales, S., Ruan, J. J., et al. 2016, *MNRAS*, 455, 1691
- Sahu, D. K., Anupama, G. C., Srividya, S., et al. 2006, *MNRAS*, 372, 1315
- Schartmann, M., Ballone, A., Burkert, A., et al. 2015, *ApJ*, 811, 155
- Schlegel, E. M. 1990, *MNRAS*, 244, 269
- Schlegel, D. J., Finkbeiner, D. P., & Davis, M. 1998, *ApJ*, 500, 525
- Shappee, B. J., Prieto, J. L., Grupe, D., et al. 2014, *ApJ*, 788, 48
- Sheng, Z., Wang, T., Jiang, N., et al. 2017, *ApJL*, 846, L7
- Sheng, Z., Wang, T., Jiang, N., et al. 2020, *ApJ*, 889, 46
- Sniegowska, M., Czerny, B., Bon, E., et al. 2020, *A&A*, 641, A167
- Stone, N. C., & Metzger, B. D. 2016, *MNRAS*, 455, 859
- Stritzinger, M., Taddia, F., Fransson, C., et al. 2012, *ApJ*, 756, 173
- Tartaglia, L., Pastorello, A., Sollerman, J., et al. 2020, *A&A*, 635, A39
- Trakhtenbrot, B., Arcavi, I., Ricci, C., et al. 2019, *Nature Astronomy*, 3, 242
- Uomoto, A. & Kirshner, R. P. 1986, *ApJ*, 308, 685
- Vanden Berk, D. E., Wilhite, B. C., Kron, R. G., et al. 2004, *ApJ*, 601, 692

- van Velzen, S., Mendez, A. J., Krolik, J. H., & Gorjian, V. 2016, ApJ, 829, 19
- van Velzen, S., Holoien, T. W.-S., Onori, F., et al. 2020, SSRv, 216, 124
- van Velzen, S., Gezari, S., Hammerstein, E., et al. 2021, ApJ, 908, 4
- van Velzen, S., Pasham, D. R., Komossa, S., et al. 2021, SSRv, 217, 63.
- Vazdekis, A., Sánchez-Blázquez, P., Falcón-Barroso, J., et al. 2010, MNRAS, 404, 1639
- Wang, J., & Merritt, D. 2004, ApJ, 600, 149
- Wang, T.-G., Zhou, H.-Y., Wang, L.-F., et al. 2011, ApJ, 740, 85
- Wang, T.-G., Zhou, H.-Y., Komossa, S., et al. 2012, ApJ, 749, 115
- Wang, T., Yan, L., Dou, L., et al. 2018, MNRAS, 477, 2943
- Wang, J., Xu, D. W., & Wei, J. Y. 2018, ApJ, 858, 49
- Wevers, T., Pasham, D. R., van Velzen, S., et al. 2019, MNRAS, 488, 4816
- Yan, L., Wang, T., Jiang, N., et al. 2019, ApJ, 874, 44
- Yang, C.-W., Wang, T.-G., Ferland, G., et al. 2013, ApJ, 774, 46
- Yip, C. W., Connolly, A. J., Vanden Berk, D. E., et al. 2009, AJ, 137, 5120
- Yang, Q., Wu, X.-B., Fan, X., et al. 2018, ApJ, 862, 109
- Yuan, W., Zhang, C., Feng, H., et al. 2015, arXiv:1506.07735
- Zabludoff, A., Arcavi, I., La Massa, S., et al. 2021, SSRv, 217, 54